Utrecht University

Debye Institute for Nanomaterials Science

Center for Extreme Matter and Emergent Phenomena

Cold Atom Nanophotonics Group

Thermalization and Gain Clamping in a Photon Bose-Einstein Condensate

Author:
M. J. Droste
4274911

Supervisors:
C. Beulenkamp B.Sc
Dr. D. van Oosten

June 21, 2018

Abstract

A system of identical bosons can exhibit a state of matter in which the ground state is macroscopically occupied. This special state is called Bose-Einstein condensation, and was predicted by Satyendra Nath Bose and Albert Einstein in 1924. It took some time before physicists achieved this experimentally, but in 1995 it was done by Eric Cornell and Carl Wieman.

Since photons are also bosonic particles, they should be able to achieve Bose-Einstein condensation in thermal equilibrium. However this is not as easy for photons as it is for atoms, since the number of photons depends on the temperature. But in 2010 the group of Martin Weitz in Bonn was able to produce a photon Bose-Einstein condensate. This was done using a dye-filled microcavity which is optically pumped.

The same principles are used in our setup. Photons inside the cavity thermalize with a fluorescent dye through multiple absorption and emission cycles. The effectively two-dimensional photon gas is trapped by a harmonic potential induced by the shape of the cavity mirrors. This results in photons with eigenenergies of the quantum harmonic oscillator. The minimal energy is determined by the cutoff frequency, set by the cavity length. The thermalization of the photon gas depends on this cutoff frequency, and the total pump power. Jonathan Keeling and Peter Kirton developed a theoretical model describing this system and its thermalization, and simulated it in one dimension.

We simulate the same model, in two dimensions using radially averaged photon modes. Threshold for Bose-Einstein condensation is determined for different cutoff frequencies. Our results show good agreement with those of Keeling and Kirton, below, at and above threshold. Multimode condensation and gain clamping of the molecular excitation density are observed above threshold. Comparison with experimental data can only be done qualitatively since it currently is uncalibrated.

Contents

1 Introduction

The development of quantum mechanics at the beginning of the 20^{th} century gave a new perspective to the understanding of physics, especially on the level of (sub)atomic particles. Moreover the theory also provided a new description of light, in terms of photons. Light was not only a wave anymore, as in Maxwells theory [1], but could also be seen as particles. Quantum mechanics also made it possible to develop quantum statistics, that emerged from the combination with statistical mechanics. In quantum statistics, indistuingishable particles in thermodynamic equilibrium occupy a certain set of discrete energy levels. This occupation can take place in two different ways, whether the particles are bosons or fermions. Fermions are described by Fermi-Dirac statistics, because they obey the Pauli exclusion principle. This principle states that identical fermions can not be in the same quantum state [2]. Particles that do not obey the Pauli exclusion principle are called bosons, and are described by Bose-Einstein statistics, developed by Satyendra Nath Bose [3] and later extended by Albert Einstein [4].

Hence identical bosons can occupy the same quantum state. Albert Einstein therefore predicted a special state of matter for a gas of bosons for sufficiently low temperatures and/or sufficiently high particle densities. In this special state, called Bose-Einstein condensation (BEC), a large fraction of the bosons in the gas occupy the lowest quantum state, or the ground state. This macroscopic occupation of the lowest energy state of the system can give rise to properties such as superfluidity [5] and superconductivity [6]. Bose-Einstein condensation was reached experimentally for the first time by Eric Cornell and Carl Wieman in 1995 [7]. Since then, BEC has been reached in several systems [8–10]. As photons are also bosonic, one could wonder whether these particles can also undergo this phase transition. However, photons are governed by Plank's law for black body radiation [11] This law states that the spectral range and the total number of photons emitted by a body depend on the temperature of that body. So when lowering the temperature of a photon gas, the total number of photons is not conserved and will also drop. Because these two parameters can not be set independently, the conditions for achieving BEC can not be met for a gas of photons. This problem has also occurred in other bosonic systems, such as exciton-polaritons in a semi-conductor microcavity [10, 12] and magnons in an Yttrium-iron-garnet (YIG) film [13]. But solutions were found, and condensation of these (quasi-)particles has been observed.

To achieve conservation of photon number in our setup an interaction medium is needed. A curved-mirror optical microcavity filled with a dye solution is used to interact with the photons. The photon gas inside the cavity thermalizes to the temperature of the dye by multiple absorption and emission cycles. So instead of photons getting absorbed by the cavity walls, the photons thermalize while conserving their total number by interaction with the dye. The curvature of the mirrors of the

cavity induces a harmonic trapping potential, and causes an effective photon mass. Since the length of the cavity is only a few wavelengths, the system is effectively two-dimensional. An optical pump is used to tune the total number of photons. The result is a thermalized two-dimensional gas of massive bosons with conserved partical number. These are the requisites for Bose-Einstein condensation. A photon BEC was first observed in Bonn by the group of Martin Weitz in 2010 [14, 15], and our setup is based on theirs.

An interesting question is how the thermalization of the photon gas depends on the intensity and size of the pump, and on the so-called cutoff frequency. Jonathan Keeling and Peter Kirton developed a theoretical model to describe the system and its thermalization [16]. In this thesis, we investigate their model by simulating it and comparing it with our experiments. In Section 2 the characteristics of a photon BEC and the theoretical model are explained. In Section 3 the experimental setup and simulations are described, and the results are analysed and discussed in Section 4.

2 Theory

2.1 Bose-Einstein Condensation of Photons

The photon condensate is achieved inside an optical microcavity. This bispherical cavity consists of two mirrors with a dye solution between them, held in place by capillary forces. The curvature of the mirrors induces a harmonic trapping potential for the photon gas, the implications of which will be discussed later in this section. The cavity is pumped by a laserbeam at an angle of 65° with respect to the optical axis, at which there is a transmission maximum through the mirrors. See Fig. 2.1 for a schematic view of the cavity. The laser is used as a photon source, and due to the high reflectivity of the mirrors, the loss of photons is minimal. The photon gas is thus confined in the cavity, and will reach thermal equilibrium by multiple absorption and emission cycles, due to which the dye acts as a heat bath. A more detailed description of this thermalization process follows in Section 2.1.3. The dye used here is Rhodamine 6G. This dye is dissolved in ethylene glycol, at concentrations between $1.5 \cdot 10^{-3}$ M and $6 \cdot 10^{-3}$ M.

The length of the cavity D_0 is a few times the wavelength of the light. This causes a large frequency spacing between longitudinal modes, i.e. a large free spectral range, comparable with the width of the spectrum shown in Fig. 2.4. This leads to spontaneous emission of photons of primarly one longitudinal mode q [15]. Hence the mode number in the longitudinal direction along the optical axis is set, which fixes one degree of freedom. This makes the photon gas effectively two dimensional, with two degrees of freedom for the transversal modes. So the system can now be formally described as a two dimensional ideal Bose gas in a harmonic trapping potential, with Bose-Einstein distributed transversal energies [14].

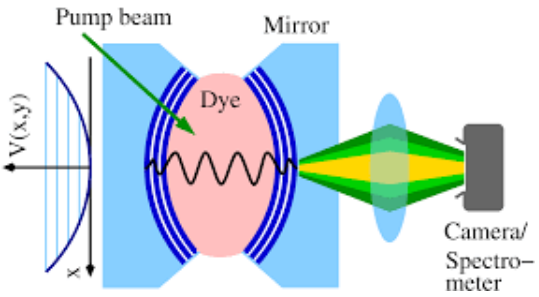

Figure 2.1: A schematic view of the dye-filled cavity. The curvature of the concave mirrors causes a harmonic trapping potential. The cavity is pumped under an angle of 65° to get maximal transmission [15].

2.1.1 Dispersion and Energies of the Photon Gas

The energy of a photon is given by $E = \hbar\omega$, where $\hbar$ is the reduced Planck constant and the angular frequency ω follows from the dispersion relation with the wavevector $\boldsymbol{k}$. Separating $\boldsymbol{k}$ in the transversal wavenumber $k_r = \sqrt{k_x^2 + k_y^2}$ and longitudinal

wavenumber k_z, the photon energy can be written as

$$E = \frac{\hbar c}{n}\sqrt{k_r^2 + k_z^2} \tag{2.1}$$

Here c is the speed of light in vacuum and n is the refractive index of the medium. Due to the curvature of the mirrors the longitudinal mode number k_z depends on the distance r from the optical axis. By the rotational symmetry in the z-direction, we can assume [14]

$$k_z = \frac{q\pi}{D(r)} \tag{2.2}$$

Where $D(r)$ is the cavity length at a distance r from the optical axis, given by

$$D(r) = D_0 - 2(R - \sqrt{R^2 - r^2}) \tag{2.3}$$

Here $D_0 = D(0)$ and R is the radius of curvature of the mirrors. Applying this and the paraxial approximation ($r \ll R, k_r \ll k_z$) to Eq. 2.1 gives [14]

$$E_{\mathrm{ph}}(\boldsymbol{r}, k_r) \simeq m_{\mathrm{ph}}\frac{c^2}{n^2} + \frac{(\hbar k_r)^2}{2m_{\mathrm{ph}}} + m_{\mathrm{ph}}r^2\frac{\Omega^2}{2} \tag{2.4}$$

This expression for the energy of the photons shows some interesting features of the system. In Eq. 2.4 we have

$$m_{\mathrm{ph}} = \frac{\pi\hbar n q}{cD_0} \tag{2.5}$$

which can be seen as the effective photon mass, and

$$\Omega = \frac{c}{n\sqrt{D_0\frac{R_0}{2}}} \tag{2.6}$$

is the trapping frequency. The energy-momentum relation above is the same as for non-relativistic massive particles with mass m_{ph} in a two-dimensional harmonic potential. So the curvature of the mirrors indeed induces a harmonic trap. Eq. 2.4 also shows a quadratic dispersion relation for the cavity photons due to the quadratic dependance on k_r, whereas photons in vacuum have linear dispersion, see Fig. 2.2.

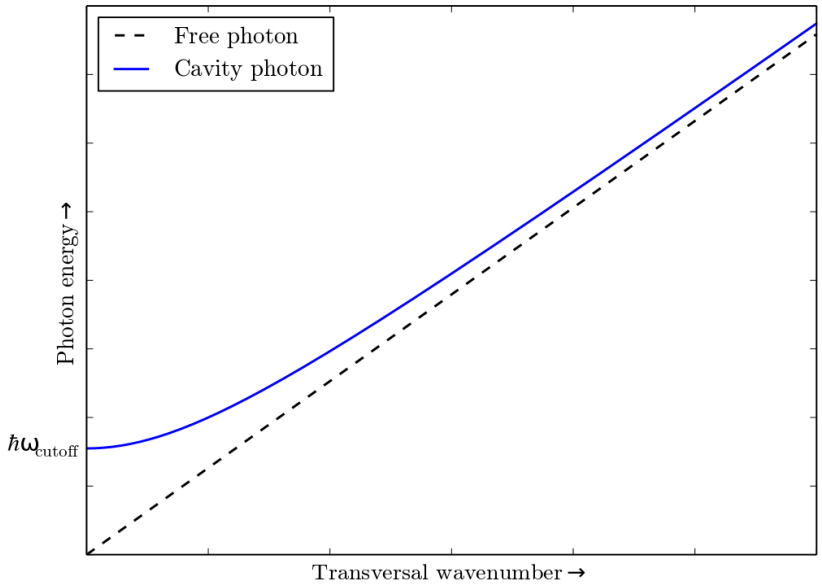

Figure 2.2: The dispersion relation for a photon in the cavity, and for a photon in vacuum [17].

The first term represents the rest energy at r=0, which is

$$E_0 \simeq m_{\text{ph}} \frac{c^2}{n^2} = \frac{\hbar c k_z(0)}{n} \tag{2.7}$$

using Eq. 2.5 and Eq. 2.2. If we define the cutoff frequency and cutoff wavelength of the cavity respectively as $\omega_c = ck_z(0)/n$ and $\lambda_c = 2\pi c/\omega_c n = 2\pi/k_z(0)$, we can write Eq. 2.7 as

$$E_0 \simeq \hbar\omega_c = \frac{hc}{n\lambda_c} \tag{2.8}$$

So the rest energy of these massive photons can be simplified into the expression above and depends on the length of the cavity, through Eq. 2.2 and Eq. 2.3. Note that this rest energy can only be reached at the center of the cavity, which is also expected for massive particles in a harmonic potential.

2.1.2 Quantum Statistical Description of the Photon Gas

Using the well-known solution of the quantum harmonic oscillator [18] we can explore the energies and their degeneracies, and subsequently the distribution of the photon gas. The transversal photon energy $u = E_{\text{ph}} - m_{\text{ph}}\frac{c^2}{n^2}$ can be calculated from Eq.

2.4. However, a particle in a two-dimensional harmonic trap has ofcourse discrete eigenenergies. The harmonic potential induced by the curvature of the mirrors can be expressed as [19]

$$V(\boldsymbol{r}) = \frac{1}{2} m_{\mathrm{ph}} \Omega^2 \boldsymbol{r}^2 \tag{2.9}$$

The transversal eigenenergies u_m due to this potential are given by

$$u_m = \hbar\Omega(m_x + m_y + 1) \tag{2.10}$$

where $m = m_x + m_y$ and $m_x, m_y \in \mathbb{N}$. These eigenenergies have a degeneracy

$$g(u_m) = 2\frac{u_m}{\hbar\Omega} \tag{2.11}$$

where the factor 2 comes from the two possible polarisation states of the photons [20].

Due to the potential in Eq. 2.9 and the non-interacting nature of photons the statistical physics of this system is best described by a two-dimensional inhomogeneous Bose gas [21]. The thermodynamics of such a system is well-known, and it shows a phase transition at low temperatures or high number densities [22]. This phase transition can be explored quantatively by looking at the expected number of photons occupying a certain transversal energy state u_m. This occupation number $n(u_m)$ is given by the degeneracy $g(u_m)$ multiplied by the Bose-Einstein distribution

$$n_{T,\mu}(u_m) = \frac{g(u_m)}{e^{\frac{u_m - \mu}{k_B T}} - 1} \tag{2.12}$$

with k_B the Boltzmann constant, T the temperature of the dye and μ the chemical potential, defined implicitly by

$$N_{\mathrm{ph}} = \sum_{u_m} n_{T,\mu}(u_m) \tag{2.13}$$

where N_{ph} is the total (average) number of photons. To solve this sum and calculate the critical photon number N_c, we explore the thermodynamic limit. In our setup $\Omega \simeq 10^{11}$ 2πHz and T is around room temperature, so $\hbar\Omega$ is small compared to $k_B T$. This implies we can treat m and therefore u_m as continuous variables, turning the sum in Eq. 2.13 into an integral and the degeneracy into the density of states.

Evaluating this integral at $\mu = 0$ gives the critical photon number [23]

$$N_c = \frac{\pi^2}{3}\left(\frac{k_B T}{\hbar\Omega}\right)^2 \tag{2.14}$$

beyond which the number of photons in the transversal energy states saturates. For $N_{\mathrm{ph}} > N_c$ a macroscopic occupation of the ground state is expected and observed [15], and so a Bose-Einstein condensate of photons is created. Using the values from our setup for Ω and T mentioned above, we find $N_c \simeq 10^5$, which can be reached experimentally.

2.1.3 Thermalization

In order to conserve the total number of photons N_{ph} in the cavity, the photon gas interacts with a dye solution by thermalization. This thermalization process is the key for achieving photon BEC. The laser beam entering the cavity acts as a pump, by exciting the dye molecules. The excited dye molecules will then emit photons, which get absorbed again by the non-excited dye molecules. By the high reflectivity of the mirrors, the photon loss is minimal, and the photon gas is confined in the cavity.

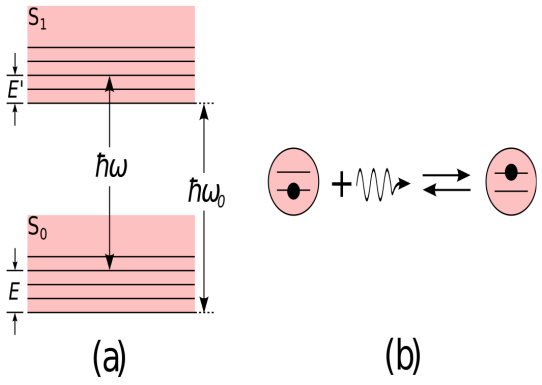

Figure 2.3: (a) Energy level scheme of a Rhodamine 6G molecule with ground state S_0 and excited state S_1. The singlets $S_{0,1}$ are manifolds containing the rovibronic substates. (b) Equilibrium reaction between the ground state and excited molecules due to photon absorption and emission [14].

The multiple absorption and emission cycles cause the photons to be in thermal contact with the dye, and adapt its temperature. These cycles are shown schematically in Fig. 2.3 in a Jablonski diagram. The manifolds contain the rovibronic substates of the dye. The dye used here is Rhodamine 6G, with the absorption and emission spectrum shown in Fig. 2.4. Due to the femtosecond timescale of the collisions, the rovibronic state of the dye molecules is almost continuously altered [24]. This process is fast enough to get absorption and emission at rovibronic states in equilibrium, which implies that the Kennard-Stepanov relation holds [25, 26]. This relation tells that absorption $\alpha(\omega)$ and emission $f(\omega)$ are related via a Boltzmann factor by $f(\omega)/\alpha(\omega) \propto \omega^3 e^{-\hbar\omega/k_B T}$ [27]. This re-

lation will later be used in Section 3.2.2 to construct a function that describes both absorption and emission.

To look quantatively at the thermalization, rate equations for the number of absorbed and emitted photons can be written down, using the Einstein coefficients A, B' and B for spontaneous emission, stimulated emission and absorption respectively [29]. From these equations the total rate equation for the number of photons $n(\omega)$ with frequency ω can be derived. Realizing that the energy of a photon is just $\hbar\omega$, results in a solution for $n(\omega)$ that is identical to the occupation number of photons with energy u_n given by Eq. 2.12 [14]. The interaction between the dye and the photon gas thus leads to a thermal distribution equal to a Bose-Einstein distribution (with a prefactor). Since we already showed in Section 2.1.2 that such a system can undergo a phase transition into a macroscopic occupation of the ground state, it is hereby shown through this thermalization process BEC can be achieved.

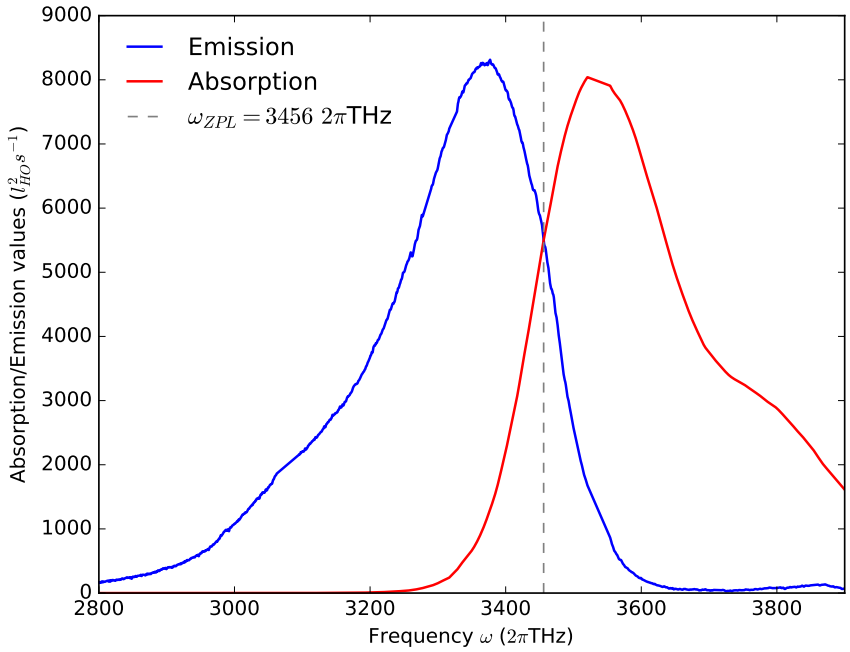

Figure 2.4: Emission and absorption spectra of Rhodamine 6G, with $\omega_{ZPL} = 3456\ 2\pi$THz. The spectra are derived from data of the group of Rob Nyman, using a cubic-spline fit [28].

The speed and degree of thermalization however depends on the emission and absorption rates of the photons. The absorption probability of a photon depends on its energy $\hbar\omega$, as shown in Fig. 2.4. For frequencies around the absorption and emission peak, these processes take place fast enough such that thermalization is completed. Thermalization can break down if absorption and emission cycles are of a timescale

comparable to $1/\kappa$, where κ is the photon loss rate. This is observed for low enough photon energies [27]. Looking at Eq. 2.8, it is clear that the minimal photon energy depends on the cutoff frequency ω_c. For ω_c far away from the peaks in Fig. 2.4, (re)absorption is reduced and thus equilibrium or rather complete thermalization, can not be reached. If the cutoff frequency is near the absorption peak, (re)absorption enhances and the photons thermalize optimally with the dye. Thus tuning ω_c determines if and how fast the photon gas thermalizes. The cutoff frequency can be tuned by changing the length of the cavity, which will be discussed in detail in Section 3.1. For our experiments, $\omega_c \simeq 3250\ 2\pi$THz, lower than the absorption peak.

2.2 Theoretical Model

Jonathan Keeling and Peter Kirton have developed a theoretical model to describe the variation in the occupation of the photon modes and the density of excited dye molecules, and their dependence on pump spot size, intensity and cutoff wavelength. This section is based on their work in [16] and [30].

2.2.1 $\Gamma(\pm\delta)$ and Photon Modes

As described in Section 2.1.2 and 2.1.3 the thermalization process by multiple absorption and emission cycles is key to achieve BEC of photons. This is shown schematically in Fig. 2.5 (a). As derived in [14], this process results in Eq. 2.12, the expected occupation number for the transversal photon energies in the cavity. The thermalization depends on the absorption and emission rates of the Rhodamine 6G molecules. It is therefore clear that these rates play an important role in whether or not equilibrium in the occupation density is reached. In general, absorption and emission for a singlet energy state of Rhodamine 6G depend on the rovibronic substates, depicted in Fig. 2.3. In earlier work [31], Keeling and Kirton eliminated these substates adiabatically, leading to a total function $\Gamma(\pm\delta)$ for absorption and emission rates of the photon modes, in which rovibrational effects are included implicitly. Here $\delta = \omega - \omega_{\mathrm{ZPL}}$ is the detuning of the photon mode with frequency ω from the Zero Phonon Line (ZPL) of the dye molecules, shown as ω_{ZPL} in Fig. 2.4. The construction of $\Gamma(\pm\delta)$ out of experimental data for absorption and emission will be discussed in Section 3.2.2. In terms of this function, the Kennard-Stepanov relation is now given by

$$\Gamma(\delta) = \Gamma(-\delta)e^{\beta\delta} \tag{2.15}$$

where $\beta = (k_B T)^{-1}$ [31].

To describe the interaction between the dye and the photons in a proper way, every photon in the cavity needs to be described by a wavefunction $\psi(\boldsymbol{r})$. Since we

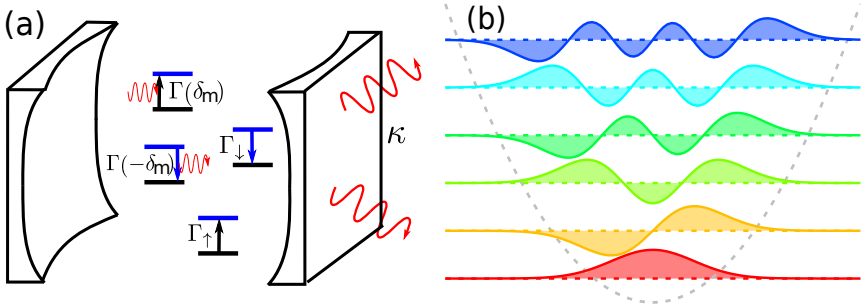

Figure 2.5: (a) Schematic view of the interaction in the cavity. $\Gamma_\uparrow$ and $\Gamma_\downarrow$ represent the absorption and emission of photons respectively, and κ is the photon loss rate. (b) The Gauss-Hermite eigenfunctions of the quantum harmonic oscillator. [16]

consider the cases with only one longitudinal mode q, whose constant effect can be absorbed in $\Gamma(\pm\delta)$ [16], we can focus on the transversal modes in the cavity. These wavefunctions or photon modes are determined by the harmonic potential of the cavity. This gives the eigenenergies from Eq. 2.10 and the Gauss-Hermite eigenfunctions as eigenstates [18], as depicted in Fig. 2.5. The photon modes $\psi_m(\boldsymbol{r})$ are thus two-dimensional Gauss-Hermite functions, with corresponding frequencies ω_m. These frequencies are harmonically spaced and determined by the longitudinal energy E_0 in Eq. 2.8 and transversal energy u_m in Eq. 2.10, which give $\omega_m = \omega_c + \Omega(m_x + m_y + 1)$ where $m = m_x + m_y$. Now we can write down the transversal photon modes for this system in general form, normalised in two dimensions

$$\psi_m(\mathbf{r}) = \frac{H_{m_x}(\frac{x}{l_{\mathrm{HO}}})H_{m_y}(\frac{y}{l_{\mathrm{HO}}})e^{-r^2/2l_{\mathrm{HO}}^2}}{l_{\mathrm{HO}}\sqrt{\pi 2^{m_x+m_y}m_x!m_y!}} \tag{2.16}$$

Here $H_m(x)$ is the m^{th} Hermite polynomial [18], $r = |\mathbf{r}|$, and l_{HO} is the harmonic oscillator length, defined by

$$l_{\mathrm{HO}} = \sqrt{\frac{\hbar}{m_{\mathrm{ph}}\Omega}} = \sqrt{\frac{\lambda_c}{4\pi n}}\sqrt[4]{\frac{qR\lambda_c}{n}} \tag{2.17}$$

This is the characteristic length scale of our system, and we will express all lengths in units of l_{HO} and d-dimensional (number)densities in units of l_{HO}^{-d}. Since the harmonic oscillator length depends on m_{ph}, it also implicitly depends on the cutoff wavelength λ_c by Eq. 2.5. The cutoff wavelength thus also sets all parameters that are expressed in terms of l_{HO}.

2.2.2 Rate Equations

Now we have described the tools and important features of our system, we can work out rate equations for the photon occupations and excited dye molecules. Keeling and Kirton first introduce a 'master equation' to represent the time evolution of the density of photons $\hat{\rho}$ in the cavity. These kind of differential equations are used to describe the time evolution of a system that can be modelled as being in a certain probabilistic combination of a discrete set of states [32]. In this case, the different states are the photon modes and their energies, and the master equation describing their occupation density is given by

$$\partial_t \hat{\rho} = \mathcal{M}_0[\hat{\rho}] + \mathcal{M}_{\text{int}}[\hat{\rho}] \tag{2.18}$$

Here $\mathcal{M}_0[\hat{\rho}]$ represents the bare part of the time evolution, containing decay and pump effects. The term $\mathcal{M}_{\text{int}}[\hat{\rho}]$ describes the photon-dye molecule interaction. From this master equation, coupled equations of motion for the photon correlation matrix $[\mathbf{n}]_{m,m'}$ and density of excited dye molecules $f(\mathbf{r})$ can be derived, within the semiclassical approximation [31]. To compare the model with experiments, these equations need to be simulated and steady state results should be derived. In order to do simulations $f(\mathbf{r})$ is discretized on a grid of N_r points, and we include the first N_m photon modes. Since $[\mathbf{n}]_{m,m'}$ is thereby a $N_m \times N_m$ matrix, this results in $N_m^2 + N_r$ coupled equations of motion that need to be solved. According to Keeling and Kirton 150 ps of simulated time requires four hours of computation time [16]. This makes it unpractical to numerically produce steady state results and look at their dependence on pump spot size, intensity and cutoff wavelength.

Therefore the "diagonal approximation" is introduced. The second term $\mathcal{M}_{\text{int}}[\hat{\rho}]$ in Eq. 2.18 describes not only molecule-photon interactions, but also includes coherence between different photon modes. The diagonal approximation neglects this intermode coherence, which results in $\mathcal{M}_{\text{int}}[\hat{\rho}] = \mathcal{M}_{\text{int}}^{\text{diag}}[\hat{\rho}]$ containing only molecule-photon interaction. This approximation is thus valid in the regime of small coherence between photon modes. The $N_m^2 + N_r$ coupled equations for $[\mathbf{n}]_{m,m'}$ and $f(\mathbf{r})$ can also be simplified using this approach. The photon correlation matrix $[\mathbf{n}]_{m,m'}$ becomes diagonal because every off-diagonal term describes coherence between different modes, which is neglected. The remaining diagonal elements $n_m = [\mathbf{n}]_{m,m}$ are equivalent to the population of photons in mode m. Defining the overlap matrix as $\mathbf{f} \equiv \int d^d\mathbf{r} f(\mathbf{r})\Psi(\mathbf{r})$ makes diagonalization possible by the fact that $[\Psi(\mathbf{r})]_{m,m'} \equiv \psi_m(\mathbf{r})\psi_{m'}(\mathbf{r})$. This results in diagonal overlap elements given by

$$f_m \equiv [\mathbf{f}]_{m,m} = \int d^d\mathbf{r} f(\mathbf{r})|\psi_m(\mathbf{r})|^2 \tag{2.19}$$

Realising that $f(\mathbf{r})$ is the density of excited dye molecules, f_m is identical to the

probability that a photon in mode m is 'close to' an excited dye molecule. These terms thus play an important role in the probability of a photon interacting with a dye molecule through absorption or emission. The diagonalization of $[\mathbf{n}]_{m,m'}$ leaves only N_m terms for the photon mode population, resulting in $N_m + N_r$ coupled equations, given by

$$\partial_t n_m = \rho_0 \Gamma(-\delta_m) f_m (n_m + 1) - [\kappa + \rho_0 \Gamma(\delta_m)(1 - f_m)] n_m \tag{2.20}$$

$$\partial_t f(\mathbf{r}) = -\Gamma_{\downarrow}^{\text{tot}}(\{n_m\}, \mathbf{r}) f(\mathbf{r}) + \Gamma_{\uparrow}^{\text{tot}}(\{n_m\}, \mathbf{r})(1 - f(\mathbf{r})) \tag{2.21}$$

Here ρ_0 is the density of dye molecules in the solvent, and κ is the decay rate of the photon modes by mirror loss (assumed constant for all modes). The other terms will be clarified below. These equations can be understood from basic physical principles of emission and absorption. The rate of change of n_m, the occupation of photon mode m, in time in Eq. 2.20 depends on the amount of photons in mode m that are emitted or absorped by dye molecules. The first term represents two emission processes, which increase the number of photons in that mode. Spontaneous emission in mode m is given by the probability that such a photon will be emitted, which is just the product of the molecule density ρ_0, the overlap term f_m for an excited molecule and the emission rate $\Gamma(-\delta_m)$ of the dye at mode frequency ω_m. Stimulated emission is represented by the same factor, multiplied by the already existing photons n_m due to the nature of this process. The second term in Eq. 2.20 represents the loss of photons in mode m, following from decay and absorption. The decay term $-\kappa n_m$ is obvious. Absorption has the same structure as stimulated emission, the probability that a photon will be absorbed multiplied by the number of photons in that mode. This probability is now given by the product of ρ_0, the overlapterm $1 - f_m$ for a ground state dye molecule and the absorption rate $\Gamma(\delta_m)$.

In Eq. 2.21, the change in the excitation density $f(\mathbf{r})$ decreases by emission and increases by absorption. The term $-\Gamma_{\downarrow}^{\text{tot}}(\{n_m\}, \mathbf{r}) f(\mathbf{r})$ describes the total decay of excited dye molecules, and $\Gamma_{\uparrow}^{\text{tot}}(\{n_m\}, \mathbf{r})(1 - f(\mathbf{r}))$ is the total excitation of ground state dye molecules, which have density $1 - f(\mathbf{r})$. Here $\Gamma_{\downarrow}^{\text{tot}}(\{n_m\}, \mathbf{r})$ and $\Gamma_{\uparrow}^{\text{tot}}(\{n_m\}, \mathbf{r})$ are the total decay and excitation rates respectively given by

$$\Gamma_{\downarrow}^{\text{tot}}(\{n_m\}, \mathbf{r}) = \Gamma_{\downarrow} + \sum_m |\psi_m(\mathbf{r})|^2 \Gamma(-\delta_m)(n_m + 1) \tag{2.22}$$

$$\Gamma_{\uparrow}^{\text{tot}}(\{n_m\}, \mathbf{r}) = \Gamma_{\uparrow}(\mathbf{r}) + \sum_m |\psi_m(\mathbf{r})|^2 \Gamma(\delta_m) n_m \tag{2.23}$$

Decay of excited molecules occurs through non-cavity decay $\Gamma_{\downarrow}$ to rovibrational states of the dye that do not take part in the thermalization process, and through stimulated

and spontaneous emission of photons. This is the same as for n_m, except for the sum over the photon modes $|\psi_m(\mathbf{r})|^2$ instead of the integrated overlap terms f_m. This indicates where in the cavity emission takes place, which is required as $f(\mathbf{r})$ depends on position. Excitation of ground state molecules happens by the pump laser, which is modelled by the pump rate $\Gamma_\uparrow(\mathbf{r})$, and by absorption of photons, that has the same structure as the emission term in Eq. 2.22.

This number of equations can be solved numerically in a reasonable time for simulated time in the order of microseconds. This allows numerically exploration of the steady state. In Section 2.3 some of the results deduced by Keeling and Kirton are shown, and in Section 4 our own results will be presented.

2.3 Steady State Results

First, we impose a Gaussian pump spot

$$\Gamma_\uparrow(\mathbf{r}) = \frac{\Gamma_\uparrow^{\text{int}}}{(2\pi\sigma_p^2)^{d/2}} e^{-\frac{\mathbf{r}^2}{2\sigma_p^2}} \tag{2.24}$$

with size σ_p, total integrated intensity $\Gamma_\uparrow^{\text{int}}$ and d the dimension. Using this shape for the pump spot, some steady state results can be derived [16].

2.3.1 Far Below Threshold

First we look at pumping far below threshold, i.e. without condensation. In this regime, both n_m and $f(\mathbf{r})$ stay relatively small, because there is more photon loss and decay of excited molecules. This gives a condition for the pump spot, given by $\Gamma_\uparrow(\mathbf{r}=0) \ll \Gamma_\downarrow$. Using this condition, the steady state of Eq. 2.20 and Eq. 2.21 far below threshold can be written as

$$n_m \simeq f_m \frac{\Gamma(-\delta_m)}{\Gamma(\delta_m) + \frac{\kappa}{\rho_0}} \qquad\qquad f(\mathbf{r}) \simeq \frac{\Gamma_\uparrow(\mathbf{r})}{\Gamma_\downarrow^{\text{tot}}(\{n_m = 0\}, \mathbf{r})} \tag{2.25}$$

If also $\frac{\kappa}{\rho_0} \ll 1$ and the Kennard-Stepanov relation $\Gamma(\delta_m) = \Gamma(-\delta_m)e^{\beta\delta_m}$ is obeyed (which we assume), then the expression for n_m simplifies to $n_m = f_m e^{-\beta\delta_m}$. The first condition represent relatively low photon loss (but still high decay of excited molecules to keep the first condition), such that reabsorption occurs multiple times before a photon is lost. Obeying the KS-relation means that absorption and emission occurs through a thermal process. Both these conditions thus result in a well thermalized photon gas, and therefore are equilibrium conditions.

We can explore this equilibrium a bit further. For large pump spots, i.e. large σ_p with respect to the spatial extension of the photon modes, the overlap terms f_m can be approximated as $f_m \simeq \frac{\Gamma_\uparrow^{\text{int}}}{\Gamma_\downarrow (2\pi\sigma_p^2)^{d/2}}$ [16]. This results in a total photon number (per unit power) depending on pump spot size

$$\frac{N_{\text{ph}}}{\Gamma_\uparrow^{\text{int}}} \simeq \frac{\sum_m f_m e^{-\beta\delta_m}}{\Gamma_\uparrow^{\text{int}}} \simeq \frac{\sum_m e^{-\beta\delta_m}}{\Gamma_\downarrow (2\pi\sigma_p^2)^{d/2}} \tag{2.26}$$

Hence for large pump spots, the number of photons per unit power is proportional to σ_p^d in equilibrium.

2.3.2 At Threshold

Now the behaviour at threshold can be explored. The threshold condition for condensation of mode m is derived in [31], and is given by

$$n_m = \frac{k_B T}{\hbar\Omega} \sim \sqrt{N_{\text{ph}}} \tag{2.27}$$

where the last relation follows from Eq. 2.14. Achieving threshold requires a certain pumping power, denoted by $\Gamma_{\uparrow,\text{thres}}^{\text{int}}$. Its value follows from time-evolving Eq. 2.20-2.23. This is done by Keeling and Kirton for $d = 1$ due to computationally expensive calculations for $d = 2$. In equilibrium the threshold condition becomes $\Gamma_\uparrow(\mathbf{r} = 0) = \Gamma_\downarrow e^{\beta\delta_c}$ where $\delta_c = \omega_c - \omega_{\text{ZPL}}$ using the equilibrium conditions mentioned before [31]. This follows from the fact that the effective chemical potential $\mu_{\text{eff}(\mathbf{r})} = \omega_{\text{ZPL}} + k_B T \log\left(\frac{\Gamma_\uparrow(\mathbf{r})}{\Gamma_\downarrow}\right)$ reaches the lowest possible photon mode ω_c in this case [30]. So the threshold pump power in thermal equilibrium is

$$\Gamma_{\uparrow,\text{eqbm}}^{\text{int}} = \sqrt{2\pi}\sigma_p \Gamma_\downarrow e^{\beta\delta_c} \tag{2.28}$$

The results of implying the threshold condition in Eq. 2.27 for different values of ω_c are shown in Fig. 2.6, together with the equilibrium result. Here the different lines correspond to certain values of $\Gamma_{\text{max}} = \max[\Gamma(\delta)]$ (red is lowest, turqoise is highest). Note however that in experiments Γ_{max} is determined by the spectrum of the dye, and can only be tuned in the given units by changing l_{HO}, so by changing ω_c.

This figure stresses the influence of ω_c on the system. The dashed line shows the equilibrium threshold pump power. At small ω_c the absorption and emission processes are too slow compared to cavity loss κ, which results in an increasing threshold power. For large ω_c the thermalization is fast enough to get close to thermal equilibrium,

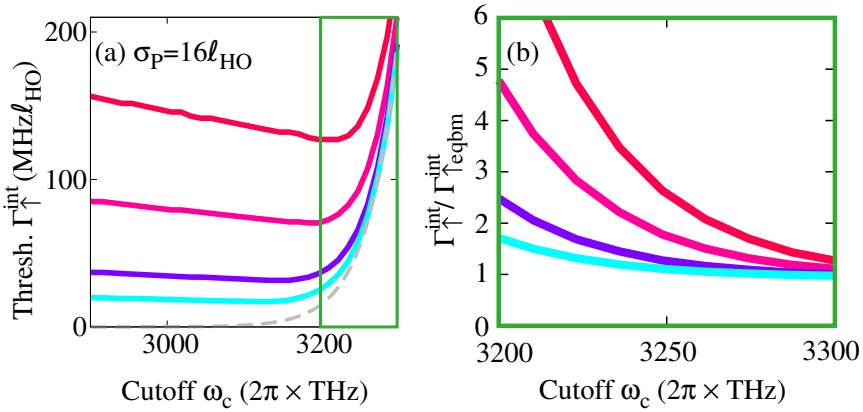

Figure 2.6: (a) Threshold pump power $\Gamma^{\text{int}}_{\uparrow,\text{thres}}$ as a function of cutoff frequency ω_c, for different values of Γ_{max}. The dashed line is the equilibrium result $\Gamma^{\text{int}}_{\uparrow,\text{eqbm}}$. (b) Ratio of $\Gamma^{\text{int}}_{\uparrow,\text{thres}}$ and $\Gamma^{\text{int}}_{\uparrow,\text{eqbm}}$, in the regime accentuated in (a). These simulations are performed in 1-D with $N_m = 200$ modes and $N_r = 300$ points [16].

which is seen by the exponential increase of $\Gamma^{\text{int}}_{\uparrow,\text{thres}}$ in Fig. 2.6(a). Physically this seems odd, since for faster thermalization one would expect to reach threshold easier. However this trend follows from the equilibrium threshold condition in Eq. 2.28, which is approached when ω_c gets closer to ω_{ZPL}. This gives of course a limitation on possible experiments, and thus ω_c will be in the regime of Fig. 2.6(b). This figure also clearly shows an asymptotic approach to $\Gamma^{\text{int}}_{\uparrow,\text{eqbm}}$, as is expected when the system gets near thermal equilibrium. Another interesting feature is the minimum in Fig. 2.6(a), which represents the easiest condensation point. This minimum is tuned by the cavity photon loss κ and Γ_{max}, and thus one of these parameters could be extracted using this point. This would be extremely useful for experiments, since κ is calculated using mirror reflection, while measuring it would give a much better result.

2.3.3 Above Threshold

At last, the steady state above threshold is studied. In equilibrium, the effective chemical potential locks at $\mu_{\text{eff}(\mathbf{r})} = \omega_c$. This occurs at threshold, and will remain the same above threshold. The general steady state result for the excitation density $f(\mathbf{r})$ by putting the time derivative to zero is

$$f(\mathbf{r}) = \frac{\Gamma^{\text{tot}}_{\uparrow}(\{n_m\}, \mathbf{r})}{\Gamma^{\text{tot}}_{\downarrow}(\{n_m\}, \mathbf{r}) + \Gamma^{\text{tot}}_{\uparrow}(\{n_m\}, \mathbf{r})} \tag{2.29}$$

Through $\Gamma^{\text{tot}}_{\uparrow}(\{n_m\}, \mathbf{r})$ this depends on the tunable parameter $\Gamma^{\text{int}}_{\uparrow}$, see Eq. 2.23. If n_m follows a Bose-Einstein distribution with chemical potential μ_{eff} and $\Gamma(\delta)$ obeys

the KS-relation, which are both equilibrium conditions, then $\Gamma(-\delta_m)(n_m+1) = \Gamma(\delta_m)n_m e^{\beta\mu}$ holds. Since we are in equilibrium in the regime above threshold, absorption and emission rates are much larger than non-cavity decay rate and pumping rate, i.e.

$$\sum_m |\psi_m(\mathbf{r})|^2 \Gamma(-\delta_m)(n_m+1) \gg \Gamma_\downarrow \tag{2.30}$$

$$\sum_m |\psi_m(\mathbf{r})|^2 \Gamma(\delta_m) n_m \gg \Gamma_\uparrow(\mathbf{r}) \tag{2.31}$$

These conditions require large $\Gamma(\pm\delta)$, since everything else is fixed. Applying this to the steady state result in Eq. 2.29 gives

$$f(\mathbf{r}) = \frac{1}{e^{-\beta\mu_{\text{eff}}}+1} = \frac{1}{e^{-\beta\delta_c}+1} \tag{2.32}$$

Hence $f(\mathbf{r})$ saturates at this distribution, which we denote by f_E. The excitation density thus becomes uniform above threshold in equilibrium, for a fixed ω_c. This kind of saturation of $f(\mathbf{r})$ is also observed for lasers [33], and is known as 'gain clamping'. Hence for a photon BEC, chemical potential locking is equivalent to the laser concept of gain clamping. This effect is seen in simulations and shown in Fig. 2.7(a).

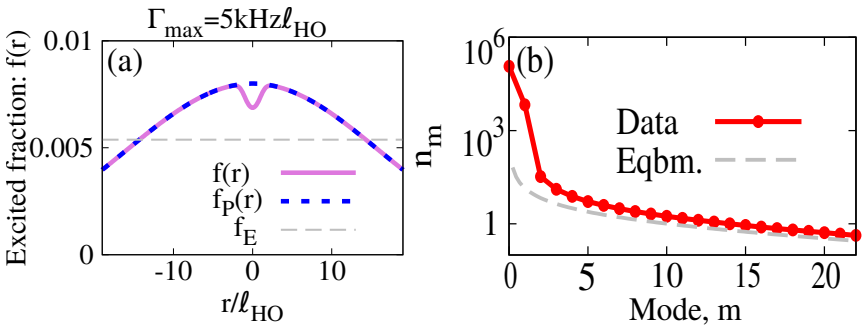

Figure 2.7: (a) Excitation density $f(\mathbf{r})$ of the dye molecules in 1-D for $\Gamma_{\max} = 5$ kHzl_{HO} and $\omega_c = 3200\ 2\pi$THz. $f_P(\mathbf{r})$ is the value set by the pump and f_E the clamped value. Imperfect gain clamping is seen in $f(\mathbf{r})$. (b) Population of photon modes n_m together with an equilibrium Bose-Einstein distribution, on logarithmic scale. This shows multimode condensation due to imperfect gain clamping. Simulations are again performed with $N_m = 200$ modes and $N_r = 300$ points [16].

However, clamping of the gain profile $f(\mathbf{r})$ is not perfect in this case. The condensed mode(s) are macroscopically occupied, which leads to a disturbance in the steady state result for $f(\mathbf{r})$, because emission and absorption rates are the highest for these modes. So $\Gamma(\pm\delta)$ is only high enough for the condensed modes, which restricts gain clamping to these modes. Since condensed mode(s) are concentrated at the center of

the harmonic trap, gain clamping is spatially restricted. So gain clamping is in this case imperfect, which is called spatial hole burning in laser terminology. As we only consider one longitudinal mode, hole burning occurs in transverse direction in the photon BEC. This can lead to multimode condensation. Because $f(\mathbf{r})$ is not uniform by its restriction, other modes can reach the threshold condition in Eq. 2.27 without being clamped. Multimode condensation is also seen in simulations, shown in Fig. 2.7(b). These effects also result in imperfect thermal equilibrium.

3 Setup

Now that we have discussed the theoretical background of the system and the model describing it, we will show our experimental setup and describe our simulations.

3.1 Experimental Setup

The heart of the setup is the dye-filled microcavity. The function of this cavity is already discussed extensively in Section 2.1. The cavity mirrors have a reflectivity of 99.9985%. Both mirrors are curved in a spherical shape with a radius of $R = 1$ m, and are a distance D_0 (see Eq. 2.3) apart. In our setup $D_0 = q\lambda_c/2n$ is around 1.5μm [19]. This leads to a trapping frequency of $\Omega \simeq 10^{11}$ 2πHz.

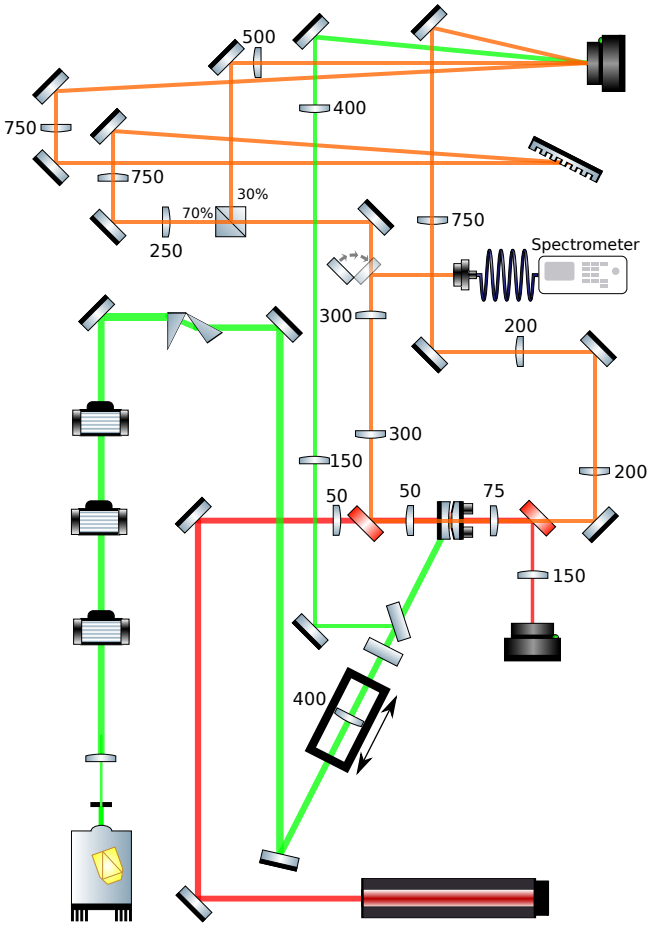

Figure 3.1: Schematic view of the setup used in our lab. Condensation is reached in the cavity by pumping with a laser. The light leaking from the mirrors is captured and send through multiple lenses and a beam splitter, and finally imaged on a CCD camera.

The microcavity is filled with Rhodamine 6G dissolved in ethylene-glycol, at concentrations $1.5 \cdot 10^{-3}$ M and $6 \cdot 10^{-3}$ M. The refractive index of the solution $n = 1.43$. The dye solution stays in the cavity by capillary forces. As can be seen in Fig. 3.1, the cavity is pumped by a green laser at 532 nm. This laser is pulsed by an AOM with a pulse length of 500 nm, and send through multiple lenses and mirrors to achieve the appropriate spot size. The thermalization process of the photon gas will now start, by which Bose-Einstein condensation can be achieved. The laserbeam enters the cavity at an angle of 65°, to reach a transmission maximum of 97% [19].

Since the mirrors are not perfectly reflective, some light will leak out. The photon loss rate is given by $\kappa = P_{loss}/t$, where $P_{loss} = 1 - 0.999985^2$ is the probability a photon will leak out of the cavity in a time $t = \frac{2D_0}{c/n} = \frac{q\lambda_c}{c}$ that it takes to traverse the cavity twice. This results in $\kappa = (1 - 0.999985^2)c/q\lambda_c$, which is around 2 THz in our setup. This leaking light is used to produce an image. On the left side in Fig. 3.1 it is send through mirrors and lenses, and a moveable mirror to measure the spectrum with a spectrometer. Later the light gets split by a beam splitter. One part is imaged directly on the CCD camera, and the other part is send through a diffraction grating. This diffraction grating spectrally separates the image, such that different photon modes get imaged at a different position, depending on their frequency. This is depicted in Fig. 3.2. Here we see the thermal cloud of photons below and above threshold, on the left and right side respectively. The yellow cone can be identified as the photon condensate. Below the separated photon modes can be seen, with the ground state on the left.

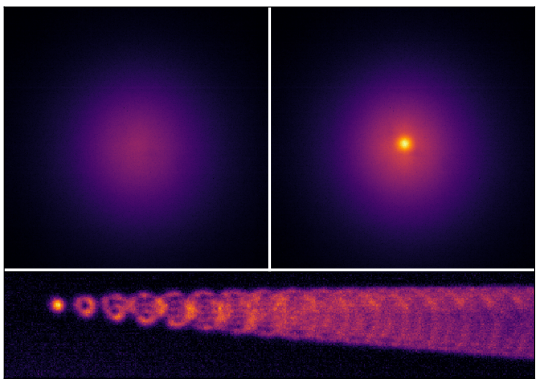

Figure 3.2: Image of the photon gas below and above threshold. The yellow pit is the photon condensate. The figure below shows the image send through the diffraction grating, which produces spectrally separated modes.

The light leaking through the other mirror also gets imaged on the CCD camera, to compare the amount of leaking through both mirrors. Furthermore, another laser beam is added to the setup. This red laser in Fig. 3.1 is a HeNe-laser, that enters the cavity on the optical axis. Its wavelength is around 632 nm, which is far above the high reflectivity range of the mirrors. This laser beam is imaged on another CCD camera. Due to the curvature of the cavity mirrors, the image shows Newton rings [34]. The radius of these HeNe-rings depends on the cavity length D_0. By setting a value for the radius of the inner ring, the cavitylength can be tuned and stabilized by comparing and changing the radius of the inner ring, using a piezo driver.

3.2 Simulations

To numerically solve the set of coupled equations in Eq. 2.20-2.23, we simulate them in Python using an adaptive time-step Runge-Kutta method. The Runge-Kutta methods are iterative methods used to solve temporal discretized ordinary differential equations [35]. This is done by using the **scipy.integrate.ode** class with **dopri5** as integrator. This integrator is an explicit Runge-Kutta method of order 4/5, and makes use of an adaptive time-step, which can be set by choosing the maximum of internally defined steps that are used [36].

3.2.1 Two Dimensional Radially Averaged Simulations

Keeling and Kirton have used the same method [16], and produced steady state results in one dimension for $N_m = 200$ modes and $N_x = 300$ grid points. For our simulations, we will also use $N_m = 200$ modes. However, our simulations will be in two dimensions using radially averaged photon modes. This means that the two dimensional transverse photon modes given in Eq. 2.16 will be averaged over their positions (x, y) for a certain distance $r = \sqrt{x^2 + y^2}$ from the center of the cavity. By the cylindrical symmetry of the cavity, this approximation is valid. This will make the calculations less computationally expensive. These new modes are of course normalized again, and will be denoted by $\rho_m(r_n)$.

Since the photon modes are radially averaged, all other positionally dependent parameters should satisfy this condition too. The discretized grid consists of $N_r = 531$ points describing a distance r from the cavity center, with a constant separating distance dr. As mentioned in Section 2.2, we express all lengths in the harmonic oscillator length $l_{\mathrm{HO}} \simeq 1\mu$m and all densities in l_{HO}^{-2}. The spatial grid extends to 35 l_{HO}, which is comparable with the spatial extension of the photon modes observed in the experiment. Hence the excitation density $f(\mathbf{r})$ is now also discretized on this new grid. The density of dye molecules ρ_0 is now a 2-D number density, given by $\rho_0 = [\mathrm{R6G}] N_A D_0 l_{\mathrm{HO}}^2$ where [R6G] is the concentration of Rhodamine 6G molecules in the solution and $N_A \simeq 6 \cdot 10^{23}$ is Avogadro's number. For parameters in our setup this results in $\rho_0 \simeq 8.8 \cdot 10^7 l_{\mathrm{HO}}^{-2}$.

Another important parameter is the overlap f_m for photon mode m, given by Eq. 2.19. Due to the shape of the cavity this integral can easiest be calculated in cylindrical coordinates. Since both $f(r, \phi, z)$ and $\rho_m(r, \phi, z)$ are radially averaged, they are independent of ϕ and z, integrating out a factor of $2\pi D_0$. Since the grid is discretized, the remaining integral over r becomes a summation over N_r points. This gives

$$f_m = 2\pi D_0 \sum_{1 \leq n \leq N_r} f(r_n) \rho_m(r_n) r_n dr \tag{3.1}$$

This is in fact nothing else than the inner product between a matrix $2\pi r_n \rho_{mn}$ where $\rho_{mn} = \rho_m(r_n)$ and a vector $\mathbf{f}_n = f(r_n)$, which results in a vector $\mathbf{f}_m$. Note that the overlap terms are dimensionless.

Furthermore a Gaussian pumpspot $\Gamma_\uparrow(\mathbf{r})$ is used, with width $\sigma_p = 10 l_{\mathrm{HO}}$ which is also used approximately in experiments.

3.2.2 Construction of $\Gamma(\delta)$

All parameters to solve Eq. 2.20-2.23 are now known or can be calculated, except the total absorption and emission function $\Gamma(\delta)$. This total spectrum contains the effects of all ro-vibrational modes, as explained in Section 2.2. This function can be constructed from experimental data for emission and absorption of Rhodamine 6G in ethylene-glycol. To compare our results with the results of [16], we use the same method as described in their appendix.

Experimental data from the group of R. Nyman [28] is used. Absorption data is given in terms of cross sections in m^2 and measured at multiple concentrations. Emission data is given in terms of counts, both for angular frequencies between 2723 2πTHz and 3918 2πTHz. Some data points are filtered out because these are at high frequencies (small wavelengths), where noise is significant. The absorption data for a dye concentration is used at a certain wavelength interval, since the spectrometer has a different optimal range for different concentrations. The emission data contains some peaks due to stray light, which are also left out. The remaining data is interpolated using a cubic-spline fit $\Gamma_{\mathrm{abs.,exp}}(\omega)$ and $\Gamma_{\mathrm{em.,exp}}(\omega)$ for the absorption and emission data respectively.

To produce a single function describing both absorption and emission, the data should be given in the same units. To write the absorption cross sections as absorption rates, they are multiplied by $c/4n$, where c is the speed of light and n the refractive index of the dye-solution. Looking at the units in Eq. 2.20, we can derive that for our 2-D simulations $[\Gamma(\delta)] = l_{\mathrm{HO}}^2 s^{-1}$. Therefore we divide the absorption rates by $D_0 l_{\mathrm{HO}}^2$, eliminating the z-dimension and resulting in the right units for our simulations. To obtain the same units for the emission data, another technique is used. Absorption and emission should be the same on the Zero Phonon Line. So we normalize $\Gamma_{\mathrm{em.,exp}}(\omega)$ such that $\Gamma_{\mathrm{em.,exp}}(\omega_{\mathrm{ZPL}}) = \Gamma_{\mathrm{abs.,exp}}(\omega_{\mathrm{ZPL}})$. The resulting fits for absorption and emission are shown in Fig. 2.4.

To combine these fits in one function, the weighted sum of both is taken, resulting in a total experimental function $\Gamma_{\mathrm{exp}}(\delta) = (\Gamma_{\mathrm{abs.,exp}}(\delta) + \Gamma_{\mathrm{em.,exp}}(\delta))/2$. This function is however not consistent with the Kennard-Stepanov relation in Eq. 2.15, which is assumed to hold [14]. Furthermore, noise is significant for large negative δ, since $\Gamma_{\mathrm{exp}}(\delta)$ is small there. To take out both problems, a new function is constructed

$$\Gamma(\delta) = \frac{1+y(\delta)}{2}\Gamma_{\exp}(\delta) + \frac{1-y(\delta)}{2}\Gamma_{\exp}(-\delta)e^{\beta\delta} \tag{3.2}$$

where $y(\delta) = (2/\pi)\arctan(\hbar\delta/k_BT)$ is a smooth interpolating function between -1 and $+1$, such that $\Gamma(\delta) \simeq \Gamma_{\exp}(-\delta)e^{\beta\delta}$ which is above the noise for large negative δ. It can easily be checked that this function satisfies the Kennard-Stepanov relation. Therefore this $\Gamma(\delta)$ is the total function that will be used in the simulations to describe both emission and absorption rates. It is shown in Fig. 3.3, as a function of ω to compare with Fig. 2.4.

We now have all the tools to numerically solve the rate equations. In Section 4 steady state results will be showed, and compared with the results of Keeling and Kirton and our own measurements.

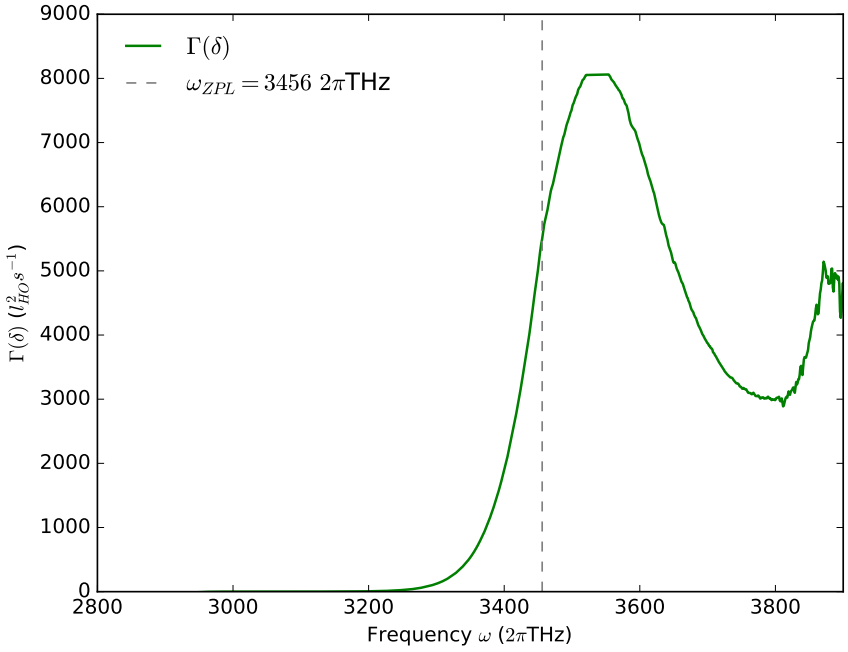

Figure 3.3: Total function $\Gamma(\delta)$ describing emission and absorption rates, constructed with experimental data. It is plotted as a function of ω to compare with Fig. 2.4. The dashed line shows the Zero Phonon Line ω_{ZPL}.

4 Results

4.1 Measurements and Settings

First we will describe the experiments performed in our lab, to explain the parameters used in the simulations. The results of these measurements will be used to compare with simulated results.

Experiments are performed in the setup described in Section 3.1, with the same parameters and dye concentrations of $1.5 \cdot 10^{-3}$ M and $6 \cdot 10^{-3}$ M. Multiple sets of measurements are done, each with a different cutoff wavelength λ_c, which is of course directly related to the cutoff frequency ω_c through Eq. 2.8. For our experiments $\lambda_c = [592 \text{ nm}, 576 \text{ nm}, 586 \text{ nm}]$, performed in the same order. The pump spot does not have a well-defined radius σ_p, since earlier experiments have shown a difference in x- and y-radius of the pumpspot. Since this value is mostly between 7 and $13 l_{\text{HO}}$, we take $\sigma_p = 10 l_{\text{HO}}$ for our simulations. Furthermore the pump spot is not controlled by a simple on/off switch, but it needs some time to increase to its total intensity $\Gamma_{\uparrow}^{\text{int}}$, and to decrease to zero. The time this process needs is about 50 ns. This is of course not included in simulations. At this moment, a new setup is build using a Pockels cell to solve this problem in the pumplaser. Measurements are done using an interleave power ramp, where pump power is increased and decreased every step. This is to exclude cumulative effects in each measurement. By the AOMs in the setup, the continuous light is cut in pulses of 500 ns. As this is much shorter than the integration time of the camera, all the measured values are effectively integrated over this period.

The settings of our simulations are based on the experiments. The used concentrations are the same, although most simulations will be done for $1.5 \cdot 10^{-3}$ M. From now on we take this concentration for our simulations, unless stated otherwise. We assume a temperature $T = 300$ K, pumpspot size $\sigma_p = 10 l_{\text{HO}}$ and $\Gamma_{\downarrow} = 250$ MHz [16, 37]. Other parameters are mentioned in Section 3. We use $N_m = 200$ photon modes and $N_r = 531$ grid points. The simulations are performed over a time $t_{\text{fin}} = 500$ ns, the same as a pulse length in the experiment, and a timestep $dt = 5$ ns for which a result is produced. The maximum of internally defined steps is $N = 4000$. Hence the simulation can take timesteps as small as 1.25 ps. Since the interaction between the photons and dye molecules occurs in the order of picoseconds [14], this is small enough to time-evolve the system accurately. The simulated results are also integrated over the period of 500 ns, and time-averaged to compare with our experimental results. In the following sections, results are shown for multiple cutoff frequencies and total pump intensities, to obtain results below, at and above threshold.

4.2 Far Below Threshold

Before comparing our simulated results with the results of Keeling and Kirton or with any measurements, we first want to check if the results of our simulations make physical sense. Therefore we look at our simulations far below threshold pumping. In Section 2.3 steady state results far below threshold are theoretically derived from Eq. 2.20-2.23. These results are given by Eq. 2.25. To simulate far below threshold, we set $\Gamma_{\uparrow}^{\text{int}} = 10^5\ l_{\text{HO}}^2$ Hz $\ll \Gamma_{\uparrow,\text{eqbm}}^{\text{int}} \ll 2\pi\sigma_p\Gamma_{\downarrow}$ where the inequality ensures that we are far below threshold. Furthermore we set $\omega_c = 3200\ 2\pi$THz and use a concentration of $1.5 \cdot 10^{-3}$ M. The result is shown in Fig. 4.1.

The molecular excitation density $f(\mathbf{r})$ is the same for both theoretical and simulated result. The photon mode occupations n_m only show a significant deviation from the theoretical result for the lowest modes. However the theoretical result shows a higher occupation of the first mode than the zeroth one. Far below threshold, the pump rate is so small with respect to the photon and non-cavity molecule loss rate, that reaching thermal equilibrium is highly unlikely. Therefore Bose-Einstein distribution of the photons can not be expected. However, since energies are very low we should still expect higher occupation of the ground state than the first excited state. So this seems to be a flaw in the theoretical approximation. We can thus conclude that our simulations are accurate.

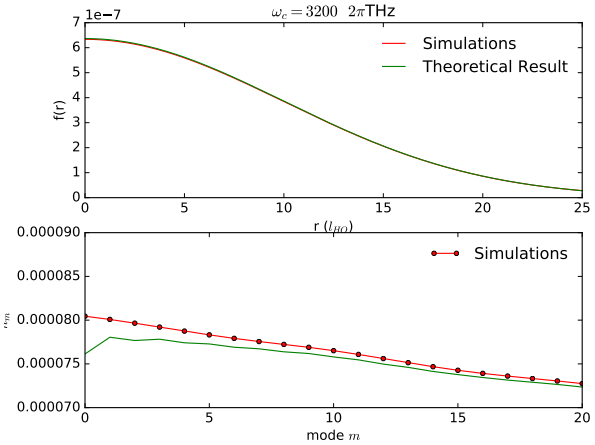

Figure 4.1: Simulated and theoretical results far below threshold. The excitation densities totally overlap, and mode occupations only differ significantly for the lowest modes.

4.3 Threshold Determination

To show results at and above threshold for different ω_c, we should first determine the threshold pump power $\Gamma_{\uparrow,\text{thres}}^{\text{int}}$ at every cutoff frequency. This is done by implying the threshold condition in Eq. 2.27 on the ground state for multiple cutoff frequencies, giving $n_0 \simeq 170$ as threshold occupation for all cutoffs. This threshold occupation is almost the same for all ω_c since Ω changes barely for different cutoff frequencies. Simulations are performed using different pump rates, until the threshold occupation was satisfied. The threshold pump power is also determined for the experiments.

These pump powers are expressed in terms of the threshold pump power in thermal equilibrium $\Gamma^{\text{int}}_{\uparrow,\text{eqbm}} = 2\pi\sigma_p^2\Gamma_\downarrow e^{\beta\delta_c}$, which is the same as Eq. 2.28, but now in two dimensions. The results are shown in Fig. 4.2.

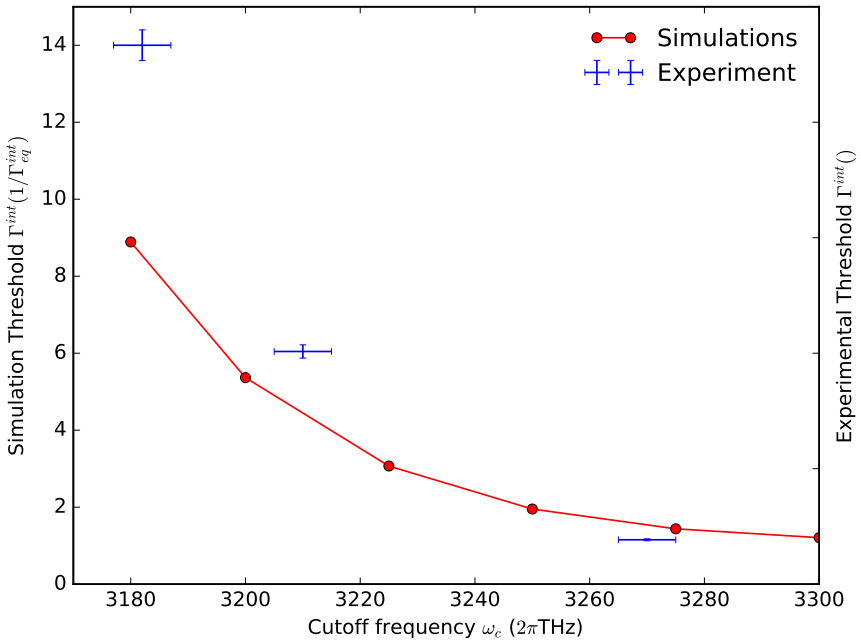

Figure 4.2: Simulated and experimental results for $\Gamma^{\text{int}}_{\uparrow,\text{thres}}$ at different ω_c, expressed in $\Gamma^{\text{int}}_{\uparrow,\text{eqbm}}$.

Thermal equilibrium is only reached for fast enough thermalization. Since thermalization is slow for ω_c further away from the Zero Phonon Line and vice versa, we can not expect to be in thermal equilibrium for every cutoff frequency. Therefore $\Gamma^{\text{int}}_{\uparrow,\text{thres}} \neq \Gamma^{\text{int}}_{\uparrow,\text{eqbm}}$, since further away from thermal equilibrium, more pumping is required to achieve Bose-Einstein condensation. It is thus also clear that $\Gamma^{\text{int}}_{\uparrow,\text{thres}}$ depends on ω_c. Since higher cutoff brings us closer to complete thermalization, we expect to approach $\Gamma^{\text{int}}_{\uparrow,\text{eqbm}}$. This is also seen in Fig. 4.2. Increasing ω_c results in an asymptotical approach of the equilibrium threshold pump power. This is seen for both simulations and experiments. The experimental data has no dimension because the pump power in our setup is currently uncalibrated. The experimental data are scaled such that it can be compared with the simulated results. Quantative claims about these results are therefore not reliable, but qualitatively there is enough to say. Both simulated and experimental results show the same asymptotic trend as depicted in Fig. 2.6(b). This figure shows the results of Keeling and Kirton for their 1-D simulation. This gives another confirmation of the working of our simulations, since these results are expected to be the same, apart from a constant factor due to different dimension. Our simulated results are also in the same order of magnitude

as those shown in Fig. 2.6(b), hence also quantatively they seem comparable.

In Section 2.3 we mentioned the significance of the minimum in Fig. 2.6(a), which represents the easiest condensation point. This minimum is tuned by the cavity photon loss κ and $\Gamma_{\max}$. Since $\Gamma_{\max}$ is set for experiments, tuning this minimum for different $\Gamma^{\text{int}}_{\uparrow,\text{eqbm}}$ could result in a far better approximation of κ. Since we've obtained a similar result for the threshold pump power, κ could be calculated by fitting this to our data. However, calibration of the pump power is first needed to make such a fit.

4.4 At Threshold

Now the threshold pump powers are determined, the actual photon occupations and excitation densities can be looked into. Results at threshold are determined for $\omega_c = 3180\ 2\pi$THz and $3275\ 2\pi$THz, corresponding to the cutoff wavelengths $\lambda_c = 592$ nm and 576 nm at which measurements are performed. The threshold pump powers for these cutoffs are $\Gamma^{\text{int}}_{\uparrow,\text{thres}} = 8.89\ \Gamma^{\text{int}}_{\uparrow,\text{eqbm}}$ and $1.438\ \Gamma^{\text{int}}_{\uparrow,\text{eqbm}}$ respectively. The results for $\omega_c = 3180\ 2\pi$THz are compared with experimental data. This is shown in Fig. 4.3 and Fig. 4.4. The green line represents the equilibrium Bose-Einstein distribution at threshold, where the chemical potential $\mu = 0$.

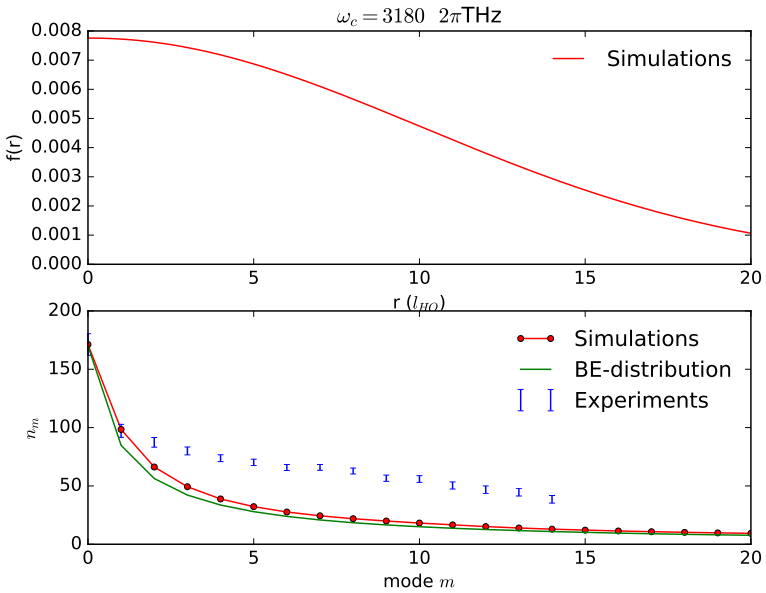

Figure 4.3: Simulated and experimental results at threshold for $\omega_c = 3180\ 2\pi$THz. The upper figure shows the excitation density $f(\mathbf{r})$, and the lower shows the mode occupations n_m. The green line is an equilibrium Bose-Einstein distribution at threshold.

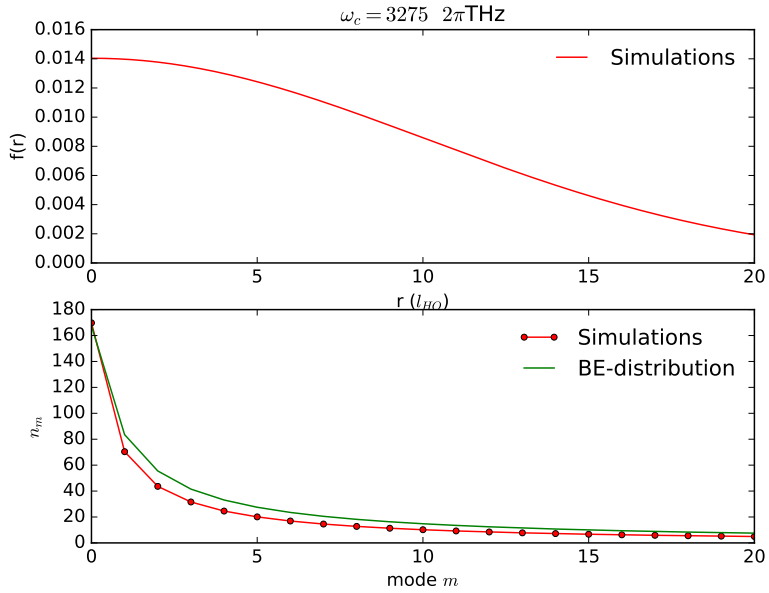

Figure 4.4: Simulated results at threshold for $\omega_c = 3275\ 2\pi$THz. The upper figure shows the excitation density $f(\mathbf{r})$, and the lower shows the mode occupations n_m. The green line is an equilibrium Bose-Einstein distribution at threshold.

The excitation density $f(\mathbf{r})$ shows a distribution expected below and at threshold [37], larger at smaller distances from the center, also shown in Fig. 2.7 as f_P. The simulated photon mode occupations n_m show the same trend as the equilibrium Bose-Einstein distribution, however it deviates at some modes. At $\omega_c = 3180\ 2\pi$THz it seems to be above equilibrium, while at $\omega_c = 3275\ 2\pi$THz it is below equilibrium. This shows again that thermal equilibrium does in fact depend on the cutoff. Of course the assumption $\mu = 0$ is not entirely accurate at threshold, since the chemical potential only approximates zero for Bose-Einstein condensation. A far more notable deviation is the one between simulations and experiments. The experimentally determined mode occupations are significantly above both simulated and equilibrium expectations, except for the ground and first excited state. Out of a set of experimental data showing the pixel counts ordered by the chemical potential of the photons in the thermal cloud, one result is chosen to compare with simulated results. This experimental result is chosen by determining the ratio between the occupation of mode $m = 0$ and mode $m = 1$. The one that shows the best agreement with the same ratio of the simulated result is used. This experimental data is then scaled to the simulated data, such that the occupation of the ground state is the same. This is done because the exact number of photons in each mode can currently not be extracted from our experimental data. Therefore, the simulations and experiments show agreement for the first two modes, but differ for other modes. Calibration of the experimental data should be done to improve data selection and make a quantitative analysis possible.

It is also interesting to look at the dependence of the threshold on concentration. For larger concentrations, the molecule density ρ_0 increases, which speeds up the thermalization process. Hence smaller threshold pump power is expected. This larger concentration will however eventually kill the dye faster, since interaction between dye molecules will become a more important factor. This increases $\Gamma_\downarrow$ and changes the emission spectrum of the dye.

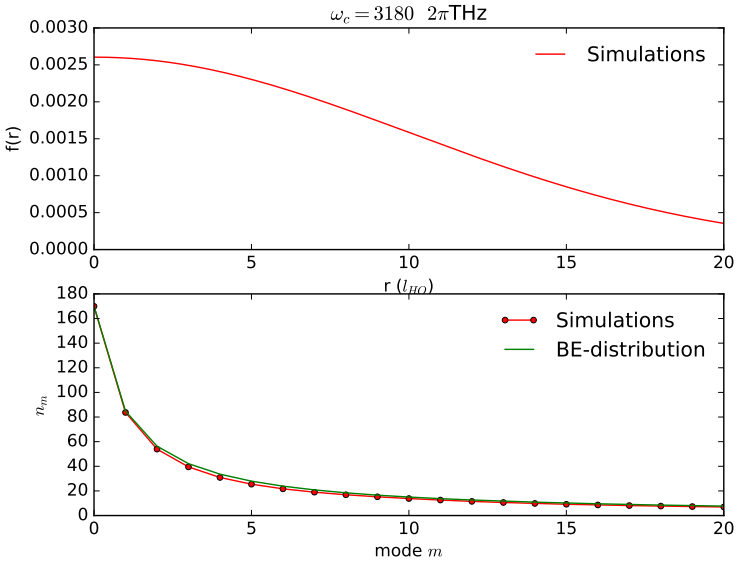

Figure 4.5: Simulated and experimental results at threshold for $\omega_c = 3180$ 2πTHz for a dye concentration of $6 \cdot 10^{-3}$ M. The upper figure shows the excitation density $f_\mathbf{r}$, and the lower shows the mode occupations n_m. The green line is an equilibrium Bose-Einstein distribution at threshold.

Fig. 4.5 shows the result for a concentration of $6 \cdot 10^{-3}$ M at threshold for $\omega_c = 3180$ 2πTHz. The threshold pump power $\Gamma^{\text{int}}_{\uparrow,\text{thres}} = 2.964\ \Gamma^{\text{int}}_{\uparrow,\text{eqbm}}$ here, which is far lower than for $1.5 \cdot 10^{-3}$ M, as expected. This concentration also shows better agreement with the equilibrium Bose-Einstein distribution at threshold, which also indicates that better thermal equilibrium is obtained when thermalization occurs faster.

4.5 Above Threshold

Finally, simulations above threshold are done, again for $\omega_c = 3180$ 2πTHz and 3275 2πTHz. Now the pump powers are chosen such that $\Gamma^{\text{int}}_\uparrow > \Gamma^{\text{int}}_{\uparrow,\text{thres}}$. We used $\Gamma^{\text{int}}_\uparrow = 9\ \Gamma^{\text{int}}_{\uparrow,\text{eqbm}}$ for $\omega_c = 3180$ 2πTHz and $\Gamma^{\text{int}}_\uparrow = 1.47\ \Gamma^{\text{int}}_{\uparrow,\text{eqbm}}$ and $1.5\ \Gamma^{\text{int}}_{\uparrow,\text{eqbm}}$ for $\omega_c = 3275$ 2πTHz. The results are shown in Fig. 4.6-4.8, with again the equilibrium Bose-Einstein distribution at threshold for comparison. For $\omega_c = 3180$ 2πTHz also experimental results are shown.

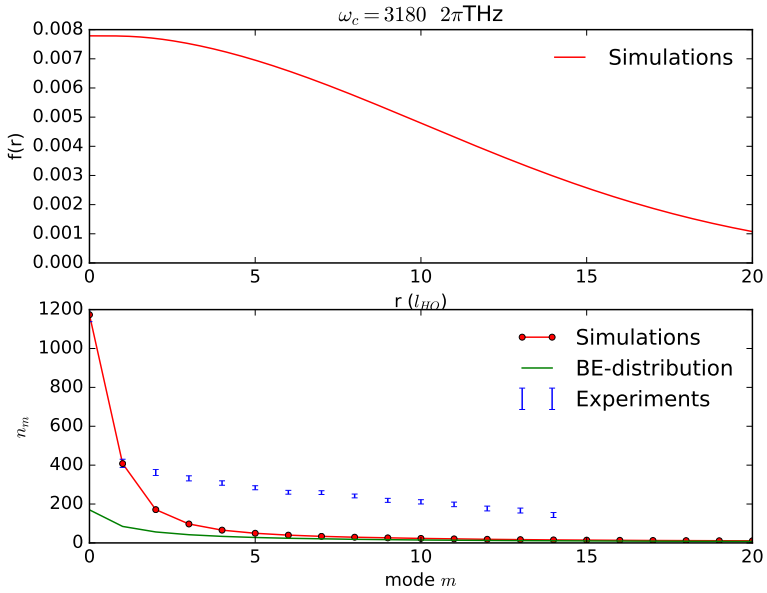

Figure 4.6: Simulated results above threshold for $\omega_c = 3180\ 2\pi$THz. The upper figure shows the excitation density $f_\mathbf{r}$, showing gain clamping. The lower figure shows the mode occupations n_m, showing multimode condensation. The green line is an equilibrium Bose-Einstein distribution at threshold.

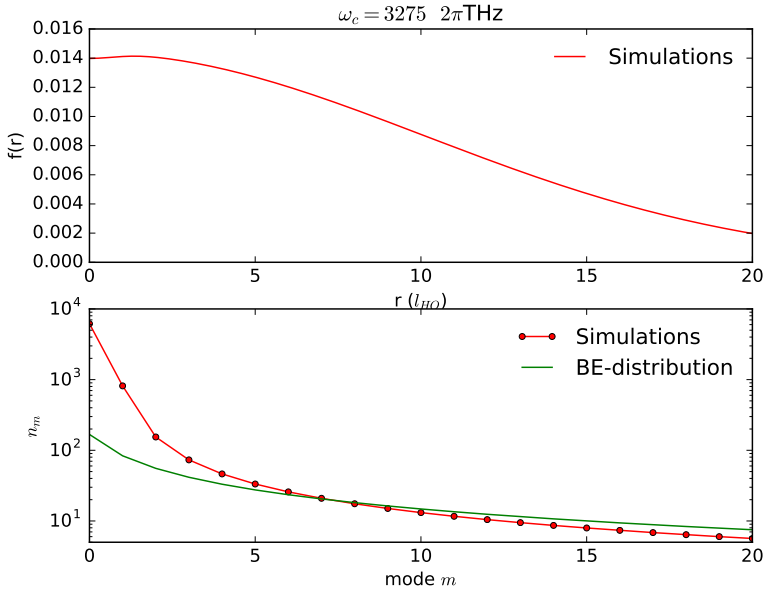

Figure 4.7: Simulated results above threshold for $\omega_c = 3275\ 2\pi$THz. The upper figure shows the excitation density $f_\mathbf{r}$, showing gain clamping. The lower figure shows the mode occupations n_m, showing multimode condensation. The green line is an equilibrium Bose-Einstein distribution at threshold.

The first two figures already show gain clamping and multimode condensation for values of $\Gamma_{\uparrow}^{\text{int}}$ just above threshold. So these effects also occur in our simulations. The gain clamping can be seen by the flattening in the excitation density, instead of smoothly growing to a maximum like what happens at threshold. The condensation of multiple photon modes occurs for both cutoffs, whereas the occupations for $\omega_c = 3275$ 2πTHz are much larger than for $\omega_c = 3180$ 2πTHz (note the logarithmic scaling). This is however hard to compare since the pumping can be harder for the first one.

The experimental data shown in Fig. 4.6 shows the same discrepancy as at threshold. Again, the ground and first excited state show good agreement with simulations, but this does not hold for other modes. This is again due to the way the data is selected. Therefore a better selection procedure should be used and the experimental data should be calibrated.

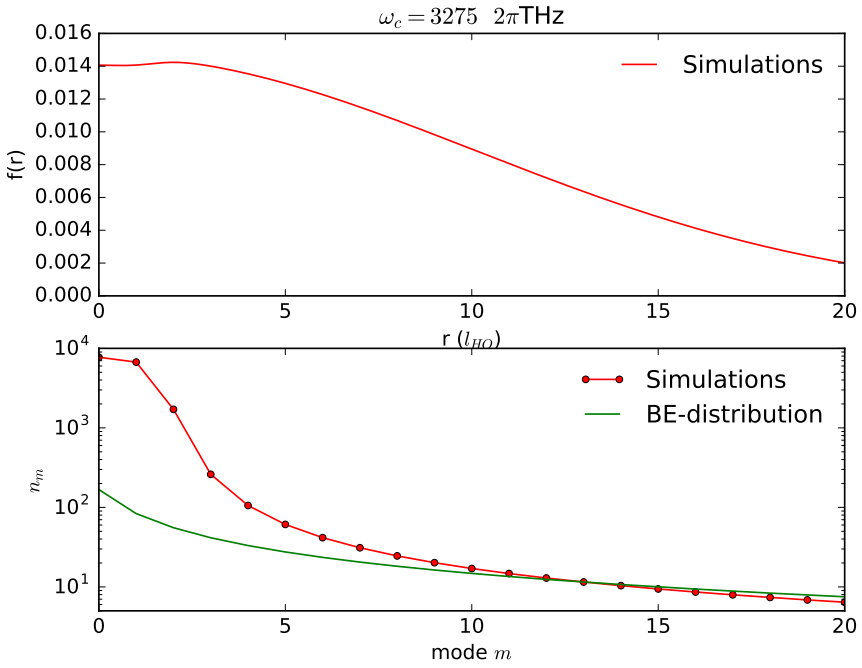

Figure 4.8: Simulated results far above threshold for $\omega_c = 3275$ 2πTHz. The upper figure shows the excitation density $f_{\mathbf{r}}$, which shows spatially restricted gain clamping. The lower figure shows the mode occupations n_m, showing multimode condensation. The green line is an equilibrium Bose-Einstein distribution at threshold.

The last figure shows results for $\omega_c = 3275$ 2πTHz far above threshold at $\Gamma_{\uparrow}^{\text{int}} = 1.5$ $\Gamma_{\uparrow,\text{eqbm}}^{\text{int}}$. Here the effect of gain clamping and multimode condensation is even more present. Occupation of other condensed modes is at the order of the occupation of the ground state. Therefore we even see a dip in the excitation density $f(\mathbf{r})$, which

is increasing to the normal density outside the spatial extension of the condensed modes. This clearly shows the spatial restriction of the gain clamping. Hence the gain clamping is indeed imperfect due to macroscopically populated modes, as shown and derived by Keeling and Kirton [16].

5 Conclusion

We have explored the thermalization of a photon Bose-Einstein condensation in a dye filled microcavity. This thermalization depends on the total pump power and the cutoff frequency, which is determined by the length of the cavity. Using our simulations of the theoretical model developed by Keeling and Kirton, the photon mode occupations and density of excited molecules are investigated. We improved their simulations by using radially averaged photon modes in two dimensions, and studied the results below, at and above threshold.

The results show the same features as their simulations, showing an agreement between the 1-D and 2-D simulations. These results contain the threshold pump powers for different cutoffs, and interesting effects above threshold like multimode condensation and gain clamping.

The mode occupations however do not seem to be in good agreement with experiments. This is due to experimental calibration and data selection problems, which should be solved in the future. One way to select data more carefully would be to look at the thermal tail of simulations and measurements instead of the occupation of the first modes.

The simulations can however be used to explore interesting areas within this subject. The position of the pumpspot could be changed, or a positionally dependent κ could be imposed. This could be interesting, since the threshold minimum depends on this photon loss, which is crucial to the experiment. Therefore accurately determining this parameter would be of great use to experiments.

6 Acknowledgements

First I would like to thank my supervisor Dr. Dries van Oosten, for giving me the opportunity to work on this project. It was very exciting to taste a bit of the experimental research done at the Debye institute, and to really take part in the current research, at the boundaries of known science. You were always available for answering questions, or discussing about the physics in our setup. I would also like to thank my daily supervisor, Charly Beulenkamp. To work with you on this project has made me enthusiastic about experimental research. Your discipline and work style inspired me, and I enjoyed our discussions about other subjects during the breaks. Furthermore I want to thank the whole Nanophotonics group to give me a little insight in your research group. You all were very kind to me, and I enjoyed doing my project here.

Appendix A : Python Code for Simulations

These are the most important parts of the Python code for simulating the rate equations. Parameters and analysis of the absorption and emission data are omitted.[1]

```
import numpy as np
import scipy.integrate as integrate
import matplotlib.pyplot as plt
import scipy.interpolate
import csv
from scipy.integrate import ode


r = np.load('theoretical_profiles_radii.npy')
#Grid points for the simulation, in radial direction (in lHO)
rhos = np.load('theoretical_profiles.npy')
#Radially averaged ho eigenstates, 0 to 35 lHO
dr = r[1]-r[0] #in lHO

for m in np.arange(rhos.shape[0]): #Normalizing wavefunctions
        rhos[m]/= np.sum(2.*pi*rhos[m]*r*dr)

degm = 2.*(m+1.) #Degeneracy of the eigenenergies of the harmonic
#oscillator, factor 2 due to polarization

def wm(m): #The frequencies of the (radially averaged) photon modes m
        return wc + (m+1.)*trapfreq
dm = wm(m) - wzpl #Detuning of the photon modes, in s^-1

#Gaussian pumpspot (pumping rate of the molecules)
pump = (gammaint/(2.*pi*sigmap**2.))*np.exp(-0.5*(r/sigmap)**2.)


#The total absorption/emission rates as function of detuning,
#gammaexp(det) is the function determined from experimental data,
#and smth(det) is a arctan.
def gamma(det):
        return ((1.+smth(det))/2.)*gammaexp(det) + ((1.-smth(det))/2.)
                *gammaexp(-det)*np.exp(det*hbar/(kB*T))
```

[1] For the 2-D averaged photon modes contact Dr. D. van Oosten: D.vanOosten@uu.nl

```
#The overlapintegrals for the excitation density and photon modes,
#as an array (no unit)!
def overlapint(f,lijst):
        modes = []
        for i in lijst:
                modes.append(np.sum(r*f*rhos[i]))
        return np.array(modes)



#Rate equations for photon mode occupation nm and
#excitation density f(r)
def ratenm(t, x):
        n = x[0:nlength]
        f = x[nlength:nlength+flength]
        fm = overlapint(f,m)*2.*pi*dr
        return rho0*gamma(-1.0*dm)*fm*(n+1) -
                (kappa + rho0*gamma(dm)*(1-fm))*n

def ratefr(t,x):
        n = x[0:nlength]
        f = x[nlength:nlength+flength]
        sum1 = np.zeros(flength)
        sum2 = np.zeros(flength)
        for i in m: #Note the degeneracies
                sum1+= rhos[i]*gamma(-1.0*dm[i])*degm[i]*(n[i]+1)
                sum2+= rhos[i]*gamma(dm[i])*degm[i]*n[i]
        return -(gammad + sum1)*f + (pump + sum2)*(1-f)



#Put the rate equations together to get one solution
def ratex(t,x):
        return np.concatenate((ratenm(t,x),ratefr(t,x)))


#Parameters for the ode solver
startvalues = F
N = 4000
tfin = 500.*10.**(-9.)
dt= 5.*10.**(-9.)
tsteps = int(tfin/dt)
```

```
#ODE solver
solver = ode(ratex)
solver.set_integrator('dopri5', nsteps=N)
solver.set_initial_value(startvalues,0)



solution=np.zeros((732,tsteps+1)) #make an 'empty' list and fill
#this with the solutions (for every timestep)
idx=0

while solver.successful() and solver.t < tfin:
        solution[0,idx]= solver.t+dt
        solution[1:,idx] = solver.integrate(solver.t+dt)
        idx+=1
```

References

[1] D. J. Griffiths, Introduction to Electrodynamics, Foruth Edition, Pearson Educataion Limited, Chap.7. (2014)

[2] D. J. Griffiths, Introduction to Quantummechanics, Second Edition, Pearson Education Limited, Chap.5, p.205-243. (2014)

[3] S. N. Bose, Plancks Gesetz und Lichtquantenhypothese, Zeitschrift für Physik, **vol. 26**, p.178-181, URL `https://link.springer.com/article/10.1007%2FBF01327326` (1924)

[4] A. Einstein, Quantentheorie des einatomigen idealen Gases, Sitzungsberichte der Preussischen Akademie der Wissenschaften. **vol. 1**, p.3. (1925)

[5] URL `https://www.nobelprize.org/nobel_prizes/physics/laureates/1996/advanced.html`

[6] J. Bardeen; L. Cooper; J. R. Schriffer, Theory of Superconductivity, Physical Review, **vol. 108, iss. 5**, URL `https://journals.aps.org/pr/abstract/10.1103/PhysRev.108.1175` (December 1, 1957)

[7] E. A. Cornell; C. E. Wieman, The Bose-Einstein condensate, Scientific American, **vol. 278, iss. 3**, p.40-45, URL `https://www.nature.com/scientificamerican/journal/v278/n3/pdf/scientificamerican0398-40.pdf` (1998)

[8] K. B. Davis et al., Bose-Einstein condensation in a gas of sodium atoms, Physical Review, **vol. 75**, p.3969-3973. (1995)

[9] C. C. Bradley; C. A. Sackett; R. G. Hulet, Bose-Einstein condensation of lithium: observation of limited condensate number, Physical Review, **vol. 78**, p.985-989. (1997)

[10] H. Deng; G. Weihs; C. Santori; J. Bloch; Y. Yamamoto, Condensation of semiconductor microcavity exciton polaritons, Science, **vol. 298**, p.199-202. (2002)

[11] D. J. Griffiths, Introduction to Quantummechanics, Second Edition, Pearson Education Limited, Chap.5, p.245-247. (2014)

[12] J. Kasprzak et al., Bose-Einstein condensation of exciton polaritons, Nature, **vol. 443**, p.409-414. (2006)

[13] S. O. Demokritov, et al., Bose-Einsteincondensation of quasi-equilibrium magnons at room temperature under pumping, Nature, **vol. 443**, p.430-433. (2006)

[14] J. Klaers; J. Schmitt; T. Damm; F. Vewinger; M. Weitz, Bose-Einstein condensation of paraxial light, Applied Physics B: Lasers and Optics, **vol 105, nr. 1**, p.17-33. (2011)

[15] J. Klaers; J. Schmitt; F. Vewinger; M. Weitz, Bose-Einstein condensation of photons in an optical microcavity, Nature **vol. 468**, p.545-548. (25 November 2010)

[16] J. Keeling; P. Kirton, Spatial dynamics, thermalization, and gain clamping in a photon condensate, Physical Review, **A 93**, 013829, URL `https://arxiv.org/abs/1506.00280` (2016)

[17] H. Jagers, Polarization of a Photon Bose-Einstein Condensate, Utrecht University Faculty of Science Theses (2016)

[18] D. J. Griffiths, Introduction to Quantummechanics, Second Edition, Pearson Education Limited, Chap.5, p.41-60. (2014)

[19] K. Perrier, Photon Bose-Einstein Condensation in a Dye-Filled Microcavity, Utrecht University Faculty of Science Theses (2016)

[20] F. van der Laan, Interaction and polarization measurements of photon Bose-Einstein condensate, Utrecht University Faculty of Science Theses (2017)

[21] P. P. V. McClintock, Ultracold quantum fields, by H.T.C. Stoof, K.B. Gubbels and D.B.M. Dickerscheid, Contemporary Physics **vol. 52, no. 2**, p.159-159. (2011)

[22] S. J. Blundell; K. M. Blundell, Concepts in Thermal Physics, Oxford University Press, Second Edition, Chap.30, p.367-372. (2010)

[23] D.S. Petrov; D.M. Gangardt; G.V. Shlyapnikov, Low-dimensional trapped gases, J. Phys. IV France **vol. 116**, p.3-44 (September 2004)

[24] K. H. Bennemann; J. B. Ketterson, Novel superfluids, Oxford University Press, **vol. 1**, (2013)

[25] E. H. Kennard, Physical Review, **vol. 29** p.466. (1927)

[26] B. I. Stepanov, Dokl. Akad. Nauk SSSR+ **vol. 112**, p.839. (1957)

[27] J. Klaers; F. Vewinger; M. Weitz, Thermalization of a two-dimensional photonic gas in a white wall photon box, Nature Physics **vol. 6**, p.512-515. (2010)

[28] R. Nyman; J. Marelic, Absorption and Fluorescence spectra of Rhodamine 6G, URL `https://zenodo.org/record/569817#.Wx-91hy-mbk` (April 2017)

[29] A. Einstein, Strahlungs-Emission und -Absorption nach der Quantentheorie, Verhandlungen der Deutschen Physikalischen Gesellschaft **vol. 18**, p.318-323.

[30] P. Kirton; J. Keeling, Nonequilibrium Model of Photon Condensation, Physical Review, **Lett. 111**, 100404, (September 2013)

[31] P. Kirton; J. Keeling, Thermalization and breakdown of thermalization in photon condensates, Physical Review, **A. 91**, 033826, (March 2015)

[32] S. Kryszewski; J. Czechowska-Kryszk, Master equation - tutorial approach, URL `arXiv:0801.1757`, (January 2008)

[33] M. Zirngibl, Gain control in erbium-doped fibre amplifiers by an all-optical feedback loop, Electronics Letters, **vol. 27, iss. 7**, p.560-561. (March 1991)

[34] G.B. Airy, VI. On the phnomena of Newton's rings when formed between two transparent substances of different refractive powers, The London, Edinburgh, and Dublin Philosophical Magazine and Journal of Science, **vol. 2, iss. 7**, p.20-30 (1833)

[35] C. Runge, Ueber die numerische Auflsung von Differentialgleichungen, Mathematische Annalen, **vol. 46, iss. 2**, p.167-178. (June 1895)

[36] URL `https://docs.scipy.org/doc/scipy/reference/generated/scipy.integrate.ode.html`

[37] H. J. Hesten; R. A. Nyman; F. Mintert, Decondensation in Nonequilibrium Photonic Condensates: When Less Is More, Physical Review Letters **120**, 040601 (January 2018)